Proceedings of The Magnetized Plasma in Galaxy Evolution
Sep. 27th – Oct. 1st 2004, Jagiellonian University, Kraków, Poland
Eds. K.T. Chyży, K. Otmianowska-Mazur, M. Soida and R.-J. Dettmar

The Radio Halo of the Starburst Galaxy NGC 253*

Volker Heesen[1], M. Krause[2], R. Beck[2], and R.-J. Dettmar[1]

[1]Astronomisches Institut der Ruhr Universität Bochum, Universitätsstr. 150, 44787 Bochum, Germany
[2]Max-Planck-Institut für Radioastronomie, Auf dem Hügel 69, 53121 Bonn, Germany

Abstract

We have conducted 3.6 cm radio continuum observations of the nearby starburst galaxy NGC 253 with the Effelsberg 100-m telescope. The polarized emission reveals a prominent radio halo with the magnetic field mainly aligned parallel to the galactic disk. We detected several radio spurs emerging from the disk into the halo. These radio spurs have no preferred alignment with respect to the nuclear starbust. Actually, they may be connected to the underlying starforming disk by a convective comic ray driven galactic wind. With recently obtained VLA-D observations at 6 cm, to be combined with Effelsberg data, we will be able to examine this connection in more detail.

1 Introduction

NGC 253 is a nearby starburst galaxy at a distance of 3.94 Mpc (Karachentsev et al. 2003). The nuclear starburst triggers a central conical outflow, which has been revealed by X-ray observations by Pietsch et al. (2000). The galaxy is highly inclined, thus it serves as one of the best examples to study in detail a prominent radio halo fuelled by an underlying starburst. A key to understand the formation of the halo is the propagation of cosmic ray (CR) electrons from the disk into the halo. Once accelerated, the cosmic rays suffer energy losses simultaneously by the competing processes of diffusion, convection, adiabatic deacceleration, and radiative cooling, e.g. synchrotron and inverse Compton (IC) losses. The nonthermal spectral index allows to investigate which process is dominating (Lerche & Schlickeiser 1982). Here we present our results emerging from an observing campaign with the Effelsberg 100-m telescope at 3.6 cm.

2 Observations and Data Reduction

The λ3.6cm (8.35 GHz) observations were performed between February 2002 and July 2004 with the single-horn receiver in the secondary focus cabin (SFK) of the 100-m Effelsberg radio telescope operated by the Max-Planck-Institut für Radioastronomie (MPIfR), Bonn. The receiver is equipped with two total power amplifiers for the left- and right-hand circularly polarized components. An IF polarimeter yields Stokes parameters Q and U simultaneously to the total intensity data. The final total intensity was CLEANed similar to the method described by Högbom (1974). The antenna pattern at λ3.6 cm was measured using 3C84. Each map was CLEANed by rotating the antenna pattern diagram (measured in the Az-El

*Based on observations with the 100-m telescope of the MPIfR (Max-Planck-Institut für Radioastronomie at Effelsberg)

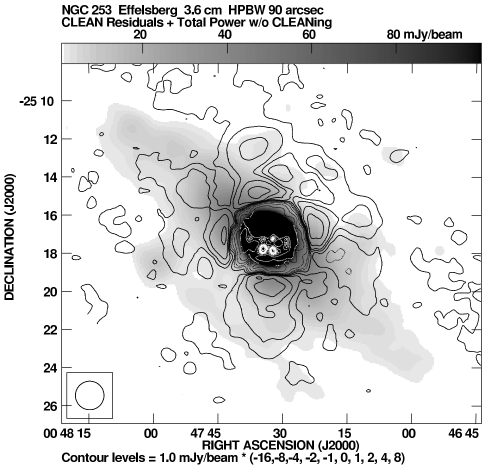

Figure 1: Contour map of the CLEANing structures, i.e. the CLEANed total power map has been subtracted from the map without CLEANing (grey scale). The Högbom CLEANing has effectively removed the sidelobes of the dirty beam which are mainly due to the strong nuclear source.

frame) according to the parallactic angle of the nucleus. This method is fully adequate in case of NGC 253 since the change of the parallactic angle across each individual map is negligible. The Högbom CLEAN technique is described in full detail by Rottmannn (1996). Our final map was produced with a clean Gaussian beam of 90" HPBW. The CLEANing structures shown in Fig. 1 underline the importance of the procedure. The prominent sidelobes are mainly due to the nuclear radio source, which has a flux of 0.98($\pm$0.05) Jy at 8350 MHz.

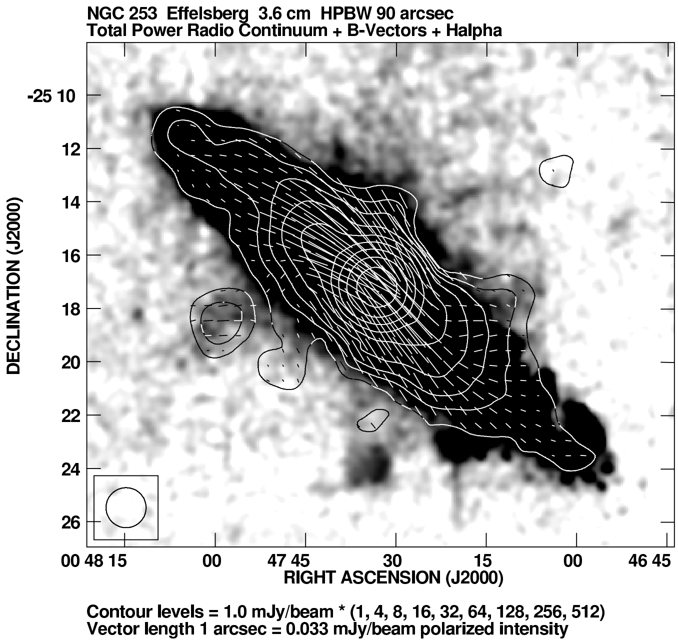

Figure 2: Total power radio continuum map at λ3.6 cm (8.35 GHz) on top of an Hα-map by Hoopes et al. (1996) which has been smoothed to 20" HPBW. The electric field vectors have been rotated by 90° to display the magnetic field orientation with the vector length proportional to the polarized emission. Note the coincidence of the Hα plumes with the radio spurs.

3 Results

Figure 2 shows the total power map at λ3.6 cm, slightly smoothed to 90" HPBW. The vectors show the magnetic field orientation with the vector length proportional to the polarized emission. The overlaid Hα map of Hoopes et al. (1996) has been smoothed to 20" HPBW to reveal the extended Hα emission. The total power emission is mainly confined to the disk with the exception of some "radio spurs" emerging into the halo. Note the coincidence of the spurs with the Hα-plumes. Moreover, there is a point like source in the southeastern outskirts of the halo. It is detached from the disk in total power. Regarding the magnetic field structure, we observe a field mainly parallel to the disk.

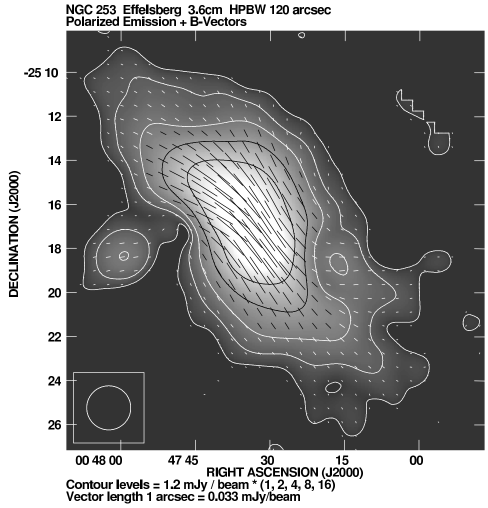

Figure 3: Linearly polarized emission of the Effelsberg λ3.6 cm observations with the magnetic field vectors. For a better signal to noise ratio, the maps have been smoothed to 120" HPBW. Two prominent radio spurs are visible where the magnetic field orientation has a strong vertical component.

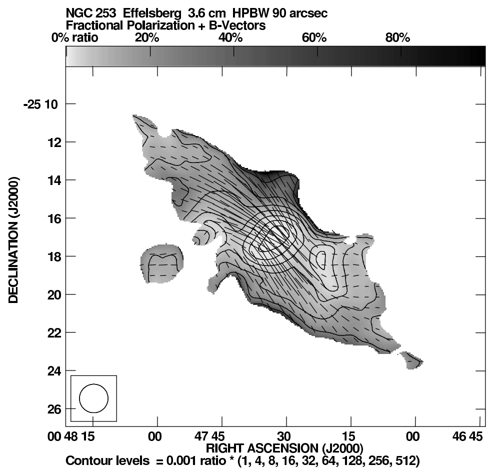

Figure 4: Fractional polarization at λ3.6 cm computed from the total power map (Fig. 2) and the map of the polarized intensity (Fig. 3). The maps have been clipped at one rms signal prior to combining. At the base of the two radio spurs prominent beam depolarization causes the dip in polarized emission and thus in the fractional polarization.

In order to investigate the magnetic field structure in more detail, we have smoothed the Q & U maps with a 120" Gaussian. The resulting map with improved signal to noise ratio reveals a very extended polarized emission (Fig. 3). The emission can now be traced much further out especially in the southern part of the halo. The polarization now reveals two prominent radio spurs, where the magnetic field has strong vertical components. Using the map of the polarized emission and the total power radio continuum we have constructed a map of the fractional polarization (Fig. 4). First, we note two deep minima at the base where the fractional polarization drops below 1%. As these minima are located at the base of the radio spurs, they can be attributed to beam depolarization.

Figure 5 shows a map of the spectral index between $\lambda 90$ cm and $\lambda 3.6$ cm. In the disk the

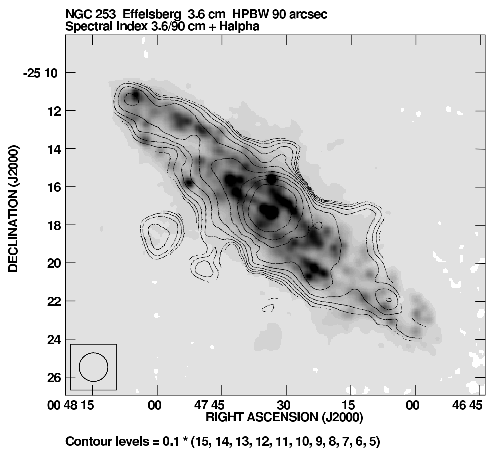

Figure 5: Spectral index map $\lambda 90/\lambda 3.6$ cm obtained from the total power maps at $\lambda 3.6$ cm (Effelsberg) and at $\lambda 90$ cm (VLA) overlaid on Hα. The spectral index α is defined by the convention of $S(\nu) \propto \nu^{-\alpha}$, with S the integrated flux and ν the observed frequency. The contours are presented in increments of 0.1 starting at 0.5 and ending at 1.5. The spectral index correlates in the disk the with the Hα emission. Additionally, there are several spurs emerging from the disk into the halo.

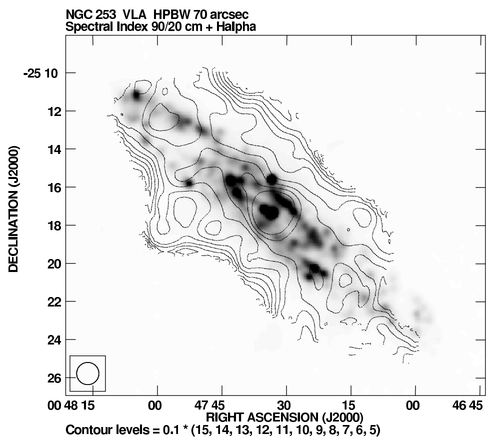

Figure 6: Spectral index map $\lambda 90/\lambda 20$ cm obtained of the VLA total power maps presented by Beck et al. (1994) on top of Hα. The contours are identical with Fig. 5. The prominent extension of flat spectral index in the south-eastern halo coincides with the radio spur of Carilli et al. (1992). To be compared with Fig. 5.

spectral index correlates with the Hα-emission, where both the northern and the southern spiral arm can be traced. Moreover, we note some extensions visible on top of that. For comparison we present a $\lambda 90/\lambda 20$ cm spectral index map performed of data presented by Beck et al. (1994) in Fig. 6, where the correlation with the underlying Hα is much weaker. The difference between the maps is obvious: the prominent extension in the $\lambda 90/\lambda 20$ cm spectral index which coincides with the radio spur of Carilli et al. (1992) has vanished in the $\lambda 3.6/\lambda 90$ cm map. On the other hand the extensions of the $\lambda 90/\lambda 3.6$ cm map are much less prominent in the $\lambda 90/\lambda 20$ cm map. This can be explained by spectral steepening as we observe at $\lambda 3.6$ cm a more aged cosmic ray electron population than at $\lambda 20$ cm.

4 Discussion

As we observe the spurs in the radio emission and polarization, cosmic ray electrons must be present in the halo. If we assume CR electrons to be injected in the disk e.g. by supernovae remnants (SNR), we can estimate a lower limit for the outflow velocity by considering the synchrotron loss time of the CR electrons. Following Beck & Krause (2005), we compute the magnetic field strength using the equipartition assumption with several simplifications: the nonthermal spectral index is fixed with $\alpha_{\rm nth} = 0.9$ and the line of sight is assumed to be 1 kpc. Using the VLA 20 cm total power, we have computed a map of the total magnetic field strength. Fig. 7 shows the magnetic field strength to be remarkably high in the halo with 10 μG at minimum. Hence, the synchrotron lifetime of cosmic ray electron reads:

$$t_{\rm syn} = \frac{8.352{\rm Gyr}}{H_\perp^2 E_0} = \frac{8.352{\rm Gyr}}{\nu(16{\rm MHz})^{0.5} B(\mu{\rm G})^{1.5}}. \tag{1}$$

With a minimum magnetic field strength of $B = 10$ μG we infer $t_{\rm syn} = 11.6$ Myr at the observing frequency $\nu = 8.35$ GHz. With the average length of the spurs of 1.5 kpc, the lower limit of the outflow velocity is $v = 130$ km/s. We can compare this number to the effective convection speed $v_{\rm con}$, which is the sum of the sound speed $c_{\rm s}$ and Alfvén speed $v_{\rm A}$. Pietsch et al. (2000) identified from the ROSAT spectral results a thin thermal plasma in the NW halo with a temperature of $T = 7.2 \times 10^4$ K and a column density of $1.3 \times 10^{20}{\rm cm}^{-2}$. The sound speed is then $c_{\rm s} = \sqrt{\gamma kT/m_{\rm H}} = 30$ km/s with $\gamma = 4/3$ being the adiabatic index of a relativistic gas. With a line of sight of 1 kpc the particle density is $n = 0.07$ cm^{-3} and the density of the thermal gas is $\rho = 1.2 \times 10^{-25}$ gcm^{-3}. With $v_{\rm A} = 80$ km/s the effective convection speed is $v_{\rm con} = c_{\rm s} + v_{\rm A} = 110$ km/s. Thus, the derived lower limit of the outflow velocity and the effective convection speed are of the same order.

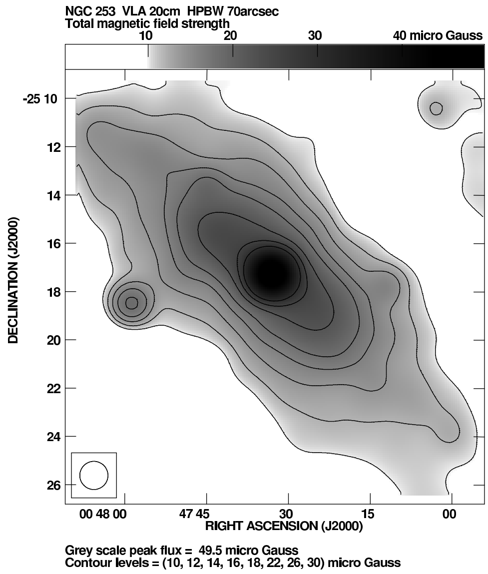

Figure 7: Total magnetic field strength obtained from the VLA total power map at λ20cm. The magnetic field strength is computed according to the equipartition assumption with a constant nonthermal spectral index of 0.9 (see text).

Hence, a pure diffusion propagation is unlikely and at least some contribution of convection to the overall CR propagation is indicated. As the energy density of the cosmic rays, the magnetic field, and the thermal gas are comparable, we have to take into account the bulk speed of the background medium. In the *chimney* model of Norman & Ikeuchi (1989) the thermal gas of the starforming is inflated by cosmic ray and magnetic pressure. The chimneys are expected to have a base size of 200 pc and a scale height of 1 kpc. Whereas our radio spurs are broader (maybe due to our beam size), their scaleheight is of the order 1 kpc in agreement with the model. We note that the observed radio spurs are not aligned with the nuclear starburst. Thus it is not likely that they are fueled by the nuclear starburst all alone. Alternatively, they may be connected to the underlying starforming disk as well.

5 Conclusions

Our new observations of the galaxy NGC 253 with the Effelsberg 100-m telescope at $\lambda 3.6$ cm reveal the emission to be well confined to the disk with the exception of several radio spurs connecting the disk with the halo. The consideration of synchrotron losses favours a convective propagation of cosmic ray particles even in the disk-halo interface. The source of cosmic ray injection – either the nuclear starburst or the starforming disk – has to be identified in the future. We expect to investigate this issue with our compiled VLA-D observations at 6 cm in more detail.

Acknowledgements

This work is partly supported by a grant of the *Deutsche Forschungs Gemeinschaft (DFG)* in the frame of the Graduiertenkolleg GRK 787 "Galaxy Groups as Laboratories for Baryonic and Dark Matter".

References

Beck, R., Carilli, C.L., Holdaway, M.A., & Klein, U., 1994, A&A, 292, 409

Carilli, C.L., Holdaway, M.A., Ho, P.T.P., & de Pree, C.G., 1992, ApJ, 399, L59

Emerson, D.T. & Graeve, R., 1988, A&A, 190, 353

Högbom, J.A., 1974, A&A Supplement, 15, 417

Hoopes, C.G., Walterbos, R.A.M., & Greenwalt, B.E., 1996, ApJ, 112, 1429

Krause, M., & Beck, R., 2005, in prep.

Lerche, I. & Schlickeiser, R., 1982, A&A, 107, 148

Norman, C.A. & Ikeuchi, S., 1989, ApJ, 345, 372

Karachentsev, I.D., Grebel, E.K., Sharina, M.E. et al., 2003, A&A, 404, 93

Rottmann, H., 1996, diploma thesis, University Bonn, Germany

Pietsch, W., Vogler, A., Klein, U., & Zinnecker, H., 2000, A&A, 360, 24